Nanoscale Advances

ROYAL SOCIETY OF CHEMISTRY

PAPER

Published on 06 November 2026
Licensed under CC-BY-NC 4.0

Check for updates

Cite this: DOI: 10.1039/d6na00760k

Droplet-to-deposit nanostructure synthesis in a fountain of backscattered electrons

Auwais Ahmed, [a] Muhamad Zakaria[a] and Andrei G. Fedorov *[ab]

Use of liquid films in liquid-phase focused electron beam induced deposition (LP-FEBID) can enable high growth rate and high purity nanostructure synthesis, but the height and aspect ratio of the deposits are limited by the liquid film thickness and by lateral spreading of reactive species. Here, we introduce a backscattered electron droplet-to-deposit (BSE-D2D) process in which a nanoelectrospray delivers metal-ion precursor containing droplets toward a grounded substrate inside a scanning electron microscope (SEM). The droplets are irradiated primarily by backscattered electrons emitted from the substrate during primary electron beam exposure. This irradiation drives radiolysis inside the droplets and reduces metal ions/ion-complexes to metal atoms before the droplets reach the substrate. Repeated delivery of these droplets leads to nanopillar growth in the direction of nanoelectrospray. The effect of electron energy on nanopillar growth was studied using Monte Carlo simulations, reaction–diffusion simulations, and experiments. Lower primary electron beam energies deliver higher backscattered electron dose to the droplets, leading to faster metal reduction and formation of larger metal nanoclusters that aggregate after reaching the substrate. At higher primary electron beam energies, lower dose delivery produces fewer and smaller reduced species, allowing metal atoms and small clusters to reorganize on the growing nanopillar into larger elongated grains. The visual invesitgation of experimentally obtained morphologies follow the proposed trend, showing a transition from nanocluster aggregation at lower energy to on-pillar metal reorganization at higher energy. These results show that BSE-D2D can extend liquid-phase FEBID to high-aspect-ratio metal nanostructures while using electron energy to influence morphology.

Received 20th August 2026
Accepted 30th October 2026

DOI: 10.1039/d6na00760k

rsc.li/nanoscale-advances

Introduction

Interaction of electrons with matter can initiate a range of physical and chemical processes that can be used for either deposition or etching of materials.[1–3] Focused Electron Beam Induced Deposition (FEBID) uses this phenomenon to deposit material with high spatial control by employing a tightly focused electron beam.[4,5] Extensive research has been carried out using focused electron beams to create materials for applications like optics, magnetics, plasmonics, and nanoelectronics.[1,6,7]

The phase of the precursor is an important consideration in FEBID. Traditionally, gas-phase precursors have been used to deposit materials such as gold,[8] silver,[9] copper,[10] and ruthenium.[11] Since FEBID is carried out in the vacuum chamber of a scanning electron microscope (SEM), the low-density gaseous precursors lead to slower deposition rates and also result in undesirable carbon co-deposition.[12,13]

Liquid-phase precursors offer the possibility of higher growth rates and higher purity, but their use comes with fundamental thermodynamic and practical challenges as it is difficult to maintain a stable liquid phase in a high-vacuum environment.[14] One approach to overcome this difficulty is to enclose the liquid inside a cell with an electron-transparent membrane.[15] This method is useful for fundamental studies, but it has important limitations for applications, including restricted choice of substrate materials which are semi-transparent to the electron beam and limited ability to create and transfer nanostructures with complex geometries. Another approach is to create liquid films inside the scanning electron microscope (SEM) by condensation in the environmental scanning electron microscope (ESEM) mode.[16] This method has also been used in combination with nanocapillaries for delivery of the liquid[17] and microwells for liquid film stabilization.[18] The main challenge in this case is the large and non-uniform thickness of the liquid film. In thick films, it is difficult for the electrons to penetrate through the liquid and reach the substrate. As a result, solid-phase nucleation preferentially initiates at the liquid-vacuum interface rather than at the liquid-substrate interface. This is undesirable because the nucleated

[a]George W. Woodruff School of Mechanical Engineering, Georgia Institute of Technology, Atlanta, GA 30332, USA. E-mail: AGF@gatech.edu

[b]Parker H. Petit Institute for Bioengineering and Biosciences, Georgia Institute of Technology, Atlanta, Georgia 30332, USA

© 2026 The Author(s). Published by the Royal Society of Chemistry

solid is influenced by liquid motion and fails to attach to the substrate.[19]

Nanoelectrospray-Assisted Focused Electron Beam Induced Deposition (NESA-FEBID) was developed to address this limitation.[20,21] In this method, an electrically biased liquid solution is electrohydrodynamically delivered to a grounded substrate, forming an ultrathin, sub-micron liquid film inside the scanning electron microscope (SEM) chamber. When a focused, high-energy electron beam passes through this thin liquid layer, there is limited electron scattering in liquid, and the deposit grows from the substrate surface, improving position control and attachment of the deposited material to the substrate. It was also shown that the addition of ammonia to an aqueous NESA-FEBID solution can decrease the surface tension, leading to thinner liquid films. Ammonia also makes the radiolytic environment more reducing, which enhances the rate of metal deposition.[19,22,23]

The BSE-D2D process uses nanoelectrospray-based charged-droplet generation developed in earlier NESA-FEBID studies[20,21] and water–ammonia chemistry established in our previous work.[19,22,23] However, the synthesis mechanism is fundamentally different. BSE-D2D uses BSEs to drive reduction within flying droplets, whereas NESA-FEBID uses the primary electron beam to irradiate a substrate-supported liquid film. The use of ultrathin films in liquid-phase (LP) FEBID improves spatial control, but it limits the height of the deposits that can be grown. Since the liquid layer must remain thin enough for the electron beam to penetrate through it, the achievable height of the deposit is constrained.[19,23] In addition, lateral diffusion of solvated electrons away from their generation region within the irradiated liquid film widens the deposits. Together, these effects limit the aspect ratio of nanostructures that can be formed using conventional LP-FEBID. BSE-D2D overcomes these limitations by using a directed stream of attoliter-scale ($\sim 10^{-18}$ L) metal-ion-precursor-containing droplets that act as mobile reaction volumes. Electron irradiation drives radiolysis and reduces metal ions within the droplets before they reach the substrate. BSEs emitted from the substrate during primary-electron-beam exposure are treated as the dominant source of this irradiation. Repeated droplet delivery allows the reduced material to accumulate in the direction of the nanoelectrospray, enabling the growth of high-aspect-ratio metallic nanostructures beyond the height limitation imposed by a stationary liquid film. Under the conditions investigated here, this process produces nanopillars extending approximately 20–40 μm from the substrate at variable angles, without their height being limited by a stationary liquid layer.

Three-dimensional, high-aspect-ratio metal structures are of interest for applications such as out-of-plane electrical interconnects, electrodes, field-emission devices, scanning probes, and sensing devices.[1,6,7] These applications require material to be deposited away from the substrate while maintaining control over the growth direction and lateral dimensions. The ability of BSE-D2D to sustain out-of-plane growth therefore makes it potentially useful for fabricating high-aspect-ratio nanostructures for these applications.

This paper focuses on fundamental mechanisms governing BSE-D2D. We examine how primary-electron energy affects the calculated BSE dose rate and predicted reduced-silver production and relate these results to the observed nanopillar morphologies and proposed growth pathways. First, the BSE-D2D FEBID process is described in detail, including the physico-chemical transformations taking place during radiolytic reduction of metal cation precursors within the droplets exposed to the BSE "fountain" emanating from the substrate. Then, the effect of electron irradiation on the BSE dose rate and metallic phase creation rate within the droplets is examined using transport-reaction modeling of reactive species generation/transport coupled to Monte-Carlo simulations of electron transport. Finally, experimental results are presented and interpreted using the insights obtained from the simulations. The paper concludes with a discussion of the key findings and recommendations for future work.

Experimental section

Droplet-to-deposit (D2D) nanopillar creation

To enable the D2D process, nanoelectrospray (NES) is used for delivery of the precursor into a vacuum deposition chamber. A negative electrical potential bias was applied to a water–ammonia silver nitrate solution loaded to the pulled capillary emitter relative to the grounded substrate. In addition to being conductive and electrically grounded, a suitable substrate should be chemically compatible with the precursor solution, solvent, and deposited material, and provide sufficient adhesion for the growing structure. The substrate should also remain stable under electron-beam irradiation and be vacuum compatible, without significant degradation, charging, or outgassing under the SEM operating conditions.

The electrohydrodynamic force draws the charged liquid in the emitter toward the grounded substrate, leading to the emission of a stream of nanodroplets. During deposition, the substrate is irradiated by the primary electron beam in scanning mode. Interaction of the primary electrons with the substrate generates a fountain of backscattered electrons (BSE) and secondary electrons (SE), which then irradiate the approaching nanodroplets in flight, as illustrated in Fig. 1(a). This electron irradiation initiates radiolysis within the nanodroplets, Fig. 1(b). This leads to the creation of radiolytic redox species within the droplet. Solvated electrons are the critical radiolytic species created in this process that reduce the silver ions/ion-complexes and create silver atoms. As silver-containing droplets land on the substrate, silver atoms aggregate on the substrate to form a nanopillar deposit. A SEM image of a D2D nanopillar formed by this process is shown in Fig. 1(c). The video of the pillar growth during the BSE-D2D is included in SI.

The rate at which silver is generated inside the droplet can be calculated using reaction–diffusion simulations.[22] A key input to this calculation is the electron dose rate delivered to the droplets.[24] During the process, droplets can encounter primary e-beam electrons, secondary electrons (SE), and backscattered electrons (BSE). The primary electrons are delivered in scanning mode, in which the e-beam rasters across the scan region pixel

© 2026 The Author(s). Published by the Royal Society of Chemistry

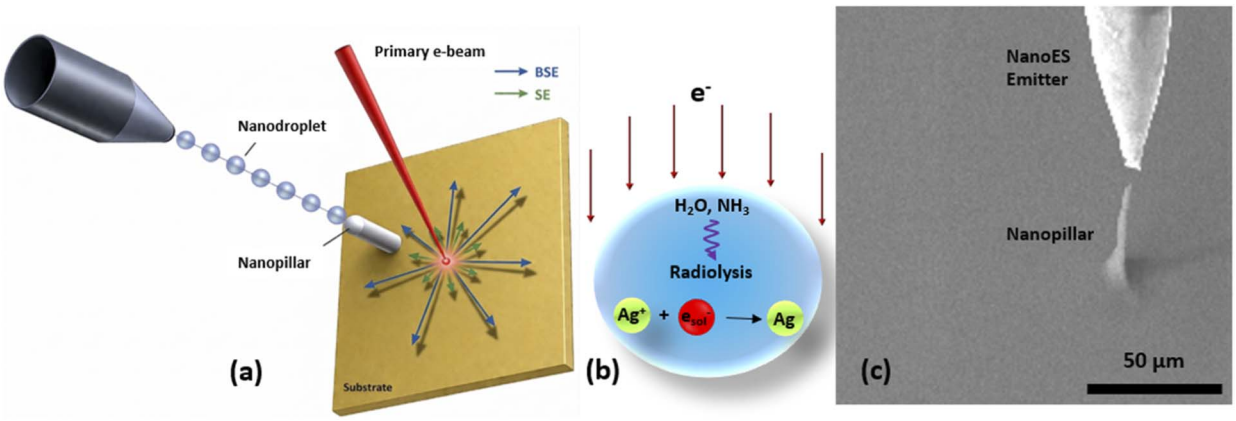


Fig. 1 Backscattered Electron Droplet-to-Deposit (BSE-D2D) process. (a) Illustration of BSE-D2D, a nanoelectrospray emitter delivers nanodroplets to the substrate. Electron beam exposure of the substrate leads to secondary electrons (SE) and backscattered electrons (BSE) generation, forming a fountain of electrons around the droplets in flight. (b) Electron irradiation of water ammonia droplets loaded with a silver nitrate precursor leads to radiolysis and generation of reactive species, including solvated electrons (e_{sol}^-), which reduce silver ions/ion complexes to metallic silver. (c) Scanning electron microscopy (SEM) image showing nanopillar growth from droplets delivered by a nanoelectrospray emitter *via* BSE-D2D process.

by pixel. The dwell time at a single pixel, 1 μs, is much longer than the total droplet flight time from the nanoelectrospray emitter tip to the substrate, ~0.4 μs (SI). This means that the maximum time for which a droplet can be exposed to the primary electron beam is limited to the time required for the droplet to pass over a single pixel, which is only a few nanoseconds (SI). Therefore, the electron dose delivered to the droplet by the primary electron beam is negligible. In contrast to the primary electrons, the droplets are continuously exposed to SE and BSE emitted from the substrate during primary electron beam irradiation. Although the SE and BSE yields are expected to be of the same order of magnitude under the conditions considered, their energy distributions are substantially different. Secondary electrons generally have energies approximately 5–100 eV, whereas the energies of the backscattered electrons extend to just below the primary beam energy. Based on these energy ranges, the short interaction time with the primary electron beam, BSE irradiation is treated as the dominant contribution to the electron dose used in the reaction–diffusion simulations.

An approximate comparison of the BSE and SE dose-rate contributions for the 3 keV primary-electron case is provided in the SI. In this calculation, the SE population is represented by a spatially uniform, normally incident flux of 25 eV electrons, and the resulting SE contribution is substantially lower than the BSE contribution under the conditions considered.

Because the BSE yield depends on the substrate material, a suitable substrate should generate sufficient BSE flux under the selected primary electron-beam conditions.

The choice of solvent is important for this process because the droplet is exposed to electron irradiation only during a short duration flight from the nanoelectrospray emitter to the substrate. For this reason, we use a water–ammonia solution containing silver nitrate precursor. As shown in our previous work,[22] the addition of ammonia changes the radiolytic redox chemistry of the silver nitrate solution to amplify the rates of silver generation. First, ammonia complexes with silver ions to form the diamine silver complex,

$$Ag^+ + 2NH_3(aq) \rightleftharpoons Ag(NH_3)_2^+$$

The silver–ammonia ion complex can then be reduced by solvated electrons to create solid silver,

$$Ag(NH_3)_2^+ + e_{sol}^- \rightarrow Ag + 2NH_3$$

In addition, hydrogen peroxide, which acts as an oxidizer of metallic silver, can also reduce the silver–ammonia ion complex providing an additional route for solid silver synthesis,

$$2[Ag(NH_3)_2]^+ + H_2O_2 \rightarrow 2Ag + 4NH_3 + 2H^+ + O_2$$

The use of ammonia therefore introduces two reduction pathways for silver formation, changing role of hydrogen peroxide as exclusively metal-oxidizing in pure water to both oxidizing and reducing in water–ammonia. Presence of ammonia also suppresses the concentration of oxidizing radiolytic species. Hydroxyl radicals are consumed by ammonia,

$$NH_3(aq) + OH^\cdot \rightarrow NH_2^\cdot + H_2O$$

and the radiolytically generated $NH_2^\cdot$ further consumes oxidizing species, including $OH^\bullet$ and dissolved oxygen,

$$NH_2^\cdot + OH^\cdot \rightarrow NH_2OH$$

$$NH_2^\cdot + O_2(aq) \rightarrow NH_2O_2$$

© 2026 The Author(s). Published by the Royal Society of Chemistry

Due to collective effect of these factors, the water–ammonia solvent makes the liquid environment electrochemically more reducing, enabling efficient in-flight creation of silver within the droplet.

Results and discussion

Simulation results

The backscattered electron (BSE) dose rate is calculated with the help of Monte Carlo simulations performed in CASINO. The substrate is modeled as a 100 nm gold layer on silicon, as shown in Fig. 2(a). The substrate is irradiated by primary electrons with energies of 20, 10, and 3 keV to obtain the BSE yield and energy spectra, shown in Fig. 2(c, e and g). The nanoelectrospray droplets are modeled as 200 nm diameter spheres and are irradiated by the BSE, Fig. 2(b). We assume that the BSE irradiation is uniformly deposited to the droplets in the direction normal to the substrate. This uniform, normally incident irradiation represents a simplifying approximation and does not account for the radial and angular BSE distribution or the movement of the BSE source during raster scanning. For each primary electron energy, the BSE spectrum was normalized by

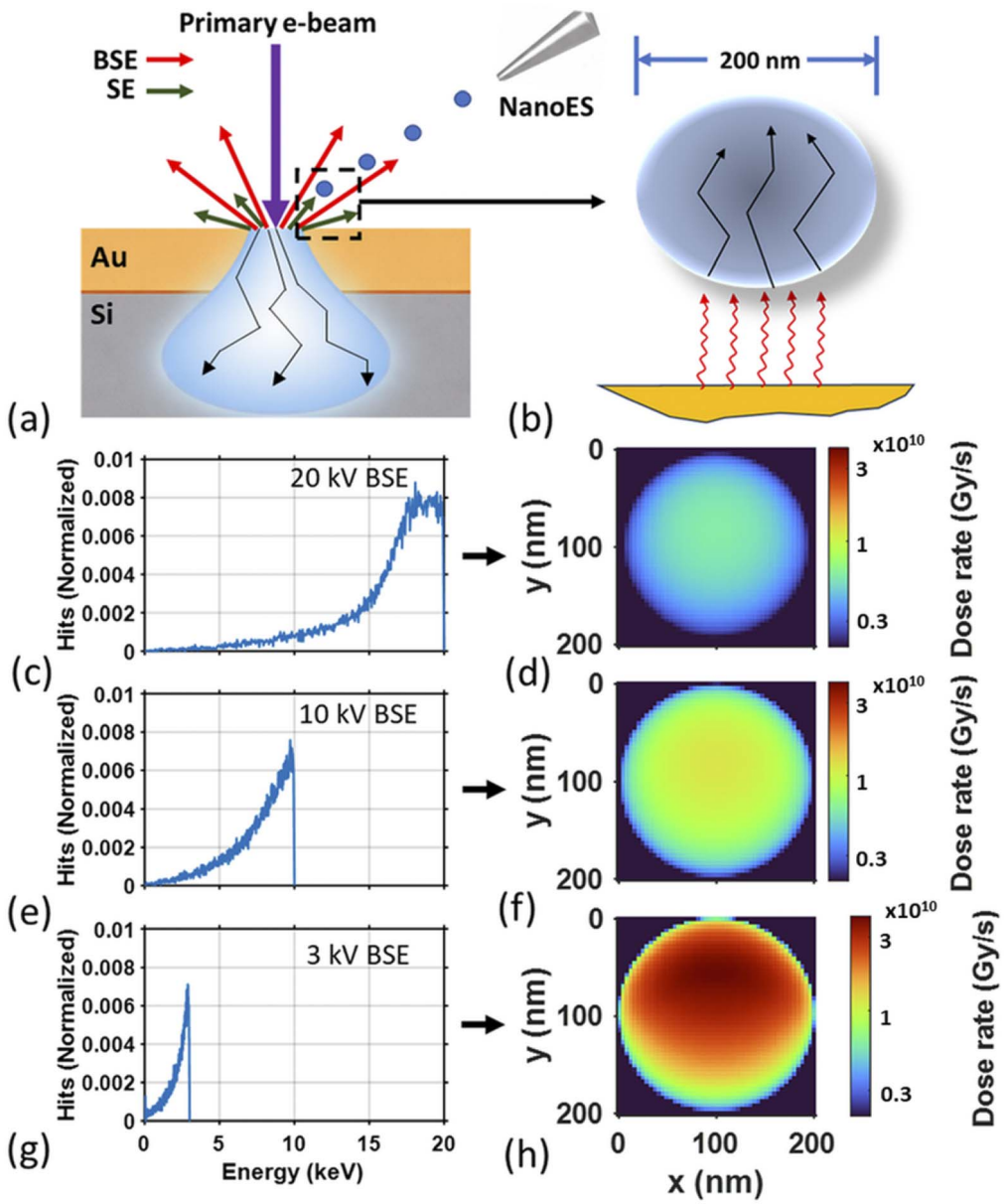


Fig. 2 Monte Carlo simulation to calculate the backscattered electron (BSE) dose rate delivered to a nanoelectrospray droplet. (a) Simulation geometry used to calculate the BSE spectra generated from a 100 nm gold layer on silicon under primary-electron irradiation. (b) Representative 200 nm-diameter spherical droplet used in the electron energy-deposition simulations. (c), (e), and (g) BSE energy spectra generated by primary electrons with energies of 20, 10, and 3 keV, respectively. "Normalized hits" denotes the number of BSE detected in each energy bin divided by the total number of BSE generated in the corresponding simulation. (d), (f), and (h) Calculated dose-rate distributions in the 200 nm droplet for BSE irradiation corresponding to primary-electron energies of 20, 10, and 3 keV, respectively.

© 2026 The Author(s). Published by the Royal Society of Chemistry

the total number of BSE generated in the simulation, such that the sum of the normalized counts over all energy bins was one. The spectrum was then divided into five groups containing approximately equal BSE populations. The weighted mean energy of each group was used as its representative BSE energy. CASINO simulations were performed at each representative energy to calculate the corresponding energy-deposition distribution in a 200 nm-diameter droplet. Each distribution was weighted by the fraction of the total BSE population contained within the corresponding energy group, the BSE coefficient, and the primary-electron rate calculated from the beam current. A detailed description of the spectrum normalization, selection of the five representative BSE energies, and conversion of the calculated energy deposition to dose rate is provided in the SI, using the 10 keV case as a representative example. The resulting BSE dose-rate distributions for primary electron energies of 20, 10, and 3 keV are shown in Fig. 2(d, f and h), respectively. Irradiation of the droplets by BSE generated from 3 keV primary electrons results in the highest deposited dose in the droplet. This is because the higher energy electrons pass through the 200 nm aqueous droplet while depositing only a small fraction of their energy within it.

A transient reaction–diffusion model is used to simulate the coupled evolution of chemical reactions and species diffusion within the droplet. The droplet is assumed to be spherical and is modeled in a 2D axisymmetric domain. Previous work has presented a detailed homogeneous reaction-network model of aqueous silver nitrate radiolysis that resolves multiple silver oxidation states, silver-cluster intermediates, and their transient concentrations.[25] In contrast, the present study uses a spatially resolved reaction–diffusion framework to predict reduced-silver production within a flying droplet but does not explicitly model subsequent nucleation, cluster growth, aggregation, or crystallization. Evaporation, advection and electromigration are neglected, and species transport is assumed to occur by Fickian diffusion. These assumptions have previously been critically assessed and shown to capture the dominant processes governing electron-mediated metallic nanomaterial synthesis in LP FEBID.[22,23] The variation of the concentration of species i C_i, with time and position is given by,

$$\frac{\partial C_i}{\partial t} = D_i\left[\frac{1}{r}\frac{\partial}{\partial r}\left(r\frac{\partial C_i}{\partial r}\right) + \frac{\partial^2 C_i}{\partial z^2}\right] + S_i + R_i$$

Here,D_i is the diffusion coefficient of species i, S_i represents the net rate of production or consumption of species i due to homogeneous chemical reactions, and R_i represents the radiolytic source term, which gives the rate of radiolytic species creation. The terms R_i and S_i are calculated following the procedure used in our previous work, using the same rate constants, diffusivities, and G-values for focused electron beam-driven water–ammonia radiolysis.[19,22] Three cases corresponding to 20, 10, and 3 keV primary electron beam irradiation are considered.

The reaction–diffusion simulations were performed in COMSOL. The silver concentration in the 200 nm axisymmetric droplets containing 5 mM silver nitrate and 10% water–ammonia was obtained at 0.4 μs, which corresponds to the time required for a droplet to travel from the nanoelectrospray emitter tip to the substrate (SI). The axisymmetric silver concentration profiles resulting from backscattered electron (BSE) irradiation corresponding to 3, 10, and 20 keV primary electrons are shown in Fig. 3. The BSE irradiation corresponding to 3 keV primary electrons results in the highest silver concentration, Fig. 3(a), with the greater enrichment of solid phase in the droplet. As the primary electron energy is increased to 10 and 20 keV, the silver concentration decreases, Fig. 3(b and c), respectively.

The simulation results suggest that the electron dose delivered to droplets during flight influences nanopillar growth pathways by affecting the silver concentration. A possible interpretation linking these simulated trends to the observed morphologies presented later in the manuscript is presented in Fig. S7.

Experimental results

The experiments were carried out in the high vacuum mode (~1 × 10^{-4} mbar) of SEM. A grounded substrate consisting of 100 nm gold deposited over silicon was used. A negative electrical bias of ~800 V was applied to a 5 mM silver nitrate solution in 10% water–ammonia to generate a negative mode nanoelectrospray. For the deposition experiments performed at primary electron energies of 3, 10, and 20 keV, the primary electron beam current was maintained at approximately 1 nA. The outlet size of the nanoelectrospray emitter is an important parameter in this process. Emitters with outlet diameters greater than 3 μm were observed to produce an expanding nanoelectrospray jet and deliver a large amount of liquid to the substrate, leading to accumulation of thick liquid films. For BSE-D2D, the droplets must follow a tight path toward the target location for nanopillar growth. At the same time, the amount of liquid reaching the substrate should remain low enough to avoid accumulation of liquid on the substrate, so that pillar growth can initiate from the point-like site on the substrate. This makes emitters with smaller outlet diameters more suitable for D2D process.

However, emitters with very small outlet diameters also create challenges. Solid material formed from silver nitrate, as well as silver reduced under electron beam irradiation, can easily clog the emitter tip. We found that emitters with outlet diameters between 1 and 2 μm provided the most suitable conditions for the conducted BSE-D2D experiments.

Within this practical emitter size range, emitter outlet size influences the droplet size, width of the nanoelectrospray jet, and liquid delivery rate, and therefore contributes to the lateral dimensions and growth rate of the D2D deposits. Larger emitter outlets generally produce an expanding jet and deliver more precursor, which can lead to structures with larger lateral dimensions, although excessive liquid delivery can prevent controlled nanopillar growth. In the present experiments, emitters with outlet diameters below 3 μm produced nanostructures with lateral dimensions ranging from a few

© 2026 The Author(s). Published by the Royal Society of Chemistry

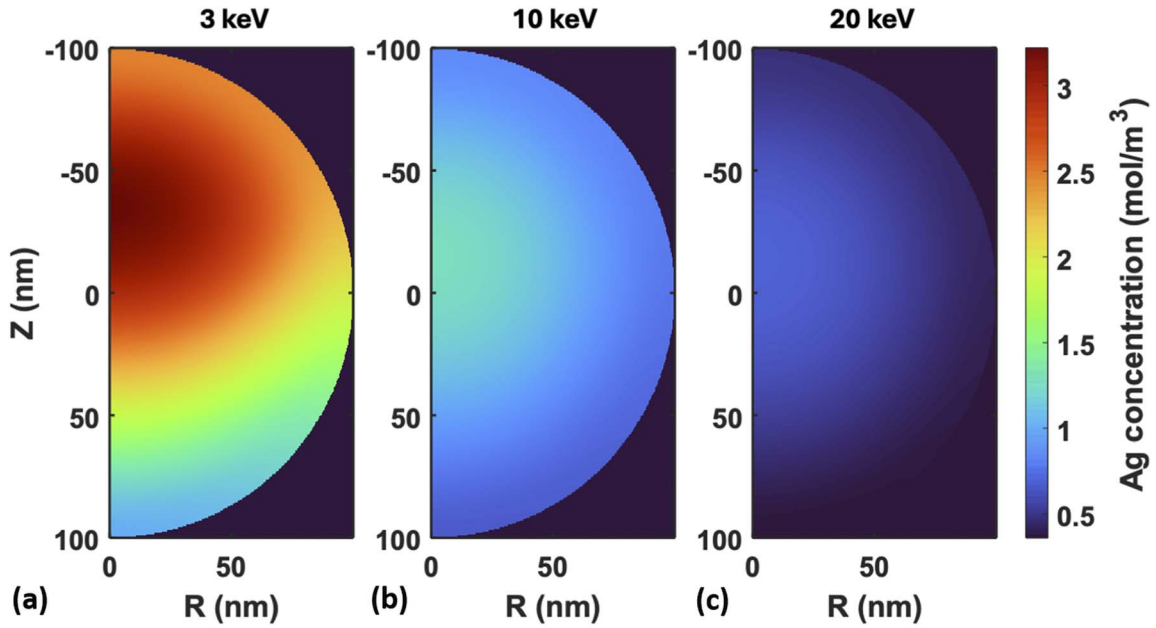


Fig. 3 COMSOL-simulated axisymmetric silver concentration in the droplet after 0.4 μs of uniform BSE irradiation. (a) Irradiation corresponding to a 3 keV primary electron beam delivers the highest dose to the droplet and results in the highest Ag concentration. For higher primary electron energies of (b) 10 keV and (c) 20 keV, the BSE dose delivered to the droplet decreases, leading to a corresponding decrease in silver concentration.

micrometers to approximately one hundred nanometers near the pillar tips.

The attainable height is influenced by the emitter-to-substrate distance, deposition duration, and precursor delivery rate. As the growing structure approaches the emitter tip, the growth rate decreases and eventually stops. The mechanical stability of the growing structure may also place a practical limit on the attainable height. Under the conditions investigated in this study, the process was therefore most suitable for forming high-aspect-ratio structures with lateral dimensions ranging from hundreds of nanometers to a few micrometers and heights of approximately 20–40 μm.

The water–ammonia, silver nitrate solution is nano-electrosprayed onto a grounded substrate in a tightly confined path. The flow rate of the nanoelectrospray is such that it does not form a liquid pool after landing on the substrate. The droplets of the nanoelectrospray are irradiated by the electrons and as a result the silver ion/ion-complexes inside the droplets are reduced to silver atoms. This reduced silver then aggregates onto the substrate leading to nanopillar deposition. Fig. 4 shows a series of nanopillars produced sequentially by moving the substrate and directing the nanoelectrospray toward a new deposition location after each nanopillar was formed. The primary aim of this study was to establish the feasibility of the BSE-D2D process and investigate the proposed growth mechanism. The parameters affecting nanopillar dimensions were not systematically controlled for a statistical reproducibility study. As a control experiment, the precursor-containing nano-electrospray was operated under otherwise identical conditions without electron-beam exposure. No nanopillar formation was observed, confirming that electron irradiation is required for BSE-D2D growth.

Experiments were conducted to synthesize nanopillars at different electron beam energies of 3, 10, and 20 keV and are shown in Fig. 5(a–c), respectively. These images also qualitatively demonstrate that off-normal nanopillar growth can be achieved by adjusting the relative orientation of the nano-electrospray emitter and substrate. All three images were acquired immediately after nanopillar deposition, before any post-deposition treatment. The nanopillar formation appears to begin with the creation of a thick base of aggregated silver on the substrate. After this base is formed, the pillar grows outward from the base in the direction of the nanoelectrospray. For the 3 keV case shown in Fig. 5(a), acquired with the substrate tilted by 45°, the pillar thickness is approximately 4.5 μm near the point where it emerges from the base. The pillar then extends to a height of approximately 30 μm. As the pillar grows, its width decreases, reaching approximately 1.5 μm near the tip. The pillar formed with 10 keV primary electron beam irradiation, Fig. 5(b), also starts with the formation of a base by aggregation of solid material. The pillar then emerges from this base with an initial width of ∼1 μm and grows to a height of ∼20 μm, with a thickness of approximately 100 nm near the tip. This pillar was straight during growth but bent after deposition due to stress accumulation or/and electrostatic interactions between the charged nanostructure stem and the substrate. The pillar formed under 20 keV irradiation grows to a height of ∼40 μm, with a width of ∼4.5 μm near the base and ∼2.5 μm near the tip, Fig. 5(c).

The height and thickness of the pillars are influenced by several experimental parameters, including the distance

© 2026 The Author(s). Published by the Royal Society of Chemistry

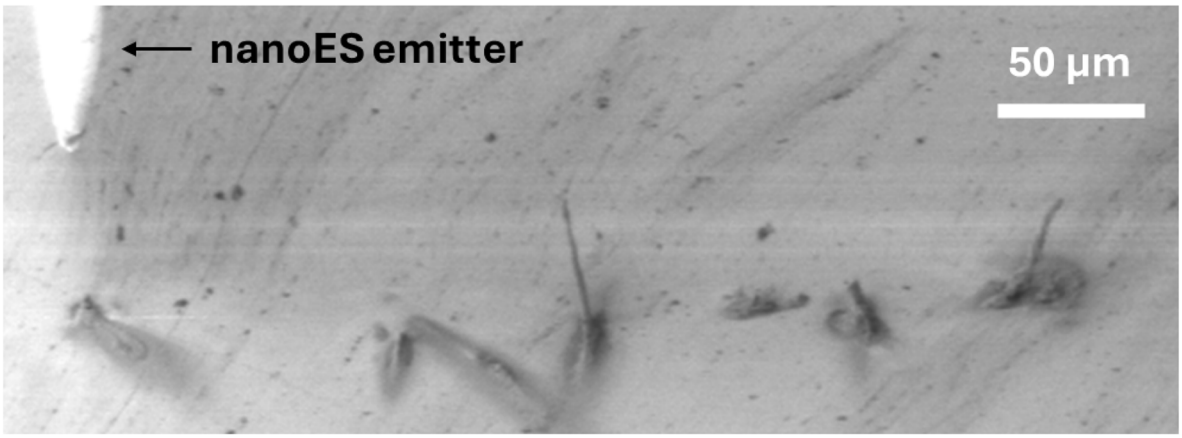


Fig. 4 Creation of BSE D2D nanopillars by experiment. A nanoelectrospray emitter electrohydrodynamically ejects charged droplets of a 10% water–ammonia solution containing 5 mM silver nitrate toward the substrate under electron beam in a scanning electron microscope (SEM). Backscattered electron irradiation of the droplets triggers radiolysis and leads to reduction of silver ions/ion-complexes to metallic silver. As droplets reach the substrate, the reduced and nucleated silver accumulates to form a nanopillar. After growth of one pillar is completed, the substrate is moved and nanoelectrospray is directed to a new location, leading to formation of another nanopillar. The figure shows a series of nanopillars created in a row in this manner (moving from right to left).

between the nanoelectrospray emitter tip and the substrate, the emitter outlet diameter, and the duration of nanoelectrospray. As the pillar height increases and it reaches closer to the emitter tip that supplies the nanoelectrosprayed precursor, the growth slows down and eventually fully stops. The emitter outlet diameter also affects the droplet size and liquid flow rate, which in turn influences the amount of precursor delivered to the growing pillar, contributing to the nanostructure size and growth rate. The as-deposited structures can contain residual precursor salt in addition to silver created *via* electron mediated reduction. Residual precursor salt remains an important limitation of the present process. Salt co-deposition can be decreased by increasing the fraction of precursor converted to metal during droplet flight through optimization of precursor concentration, solvent composition, droplet size, and electron dose. Potentially, the nanobath step could be combined with the D2D synthesis step for *in operando* excess salt removal during the nanostructure growth. To better analyze the silver deposits created by electron-mediated processes, it is important to remove the excess silver nitrate from the pillar. For this purpose, we developed a "nanobath" method to wash away the silver nitrate from the nanopillars *in situ* within the deposition chamber as a post-deposition step of BSE-D2D process. In this method, acetic acid solution is nanoelectrosprayed onto the nanopillar site. Emitters with larger outlet diameters (>5 μm) are used so that a thick acetic acid film forms around the nanopillar. The acetic acid dissolves the silver nitrate present in the nanopillar and leaves behind the silver created *via* electron-mediated reduction.

The nanobath process for a nanopillar deposited at 20 keV primary electron beam energy is shown in Fig. 6. The figure shows the time sequence from left to right. In the first two frames, Fig. 6(a and b), nanoelectrospray creates a pool of acetic acid around the pillar. In Fig. 6(c), the nanopillar breaks and falls onto the substrate. Dissolution of residual silver nitrate may contribute to this structural collapse. However, additional

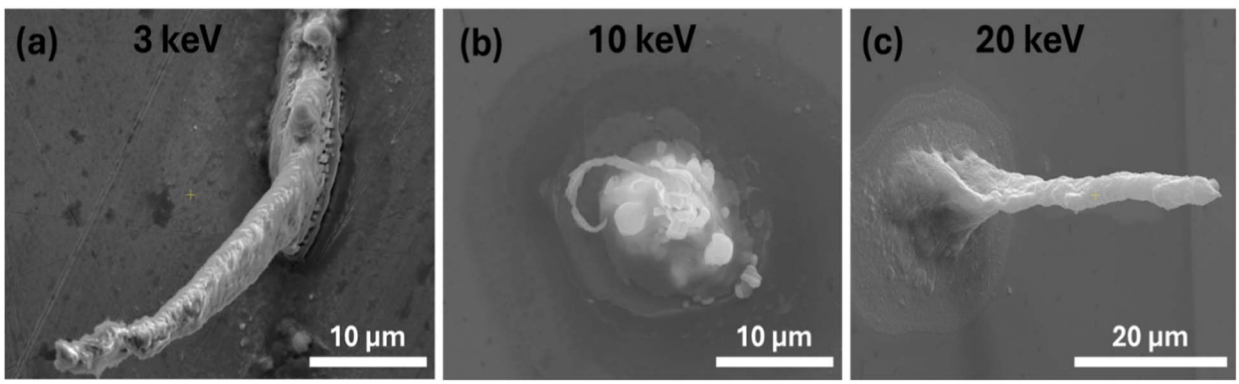


Fig. 5 Scanning electron microscopy (SEM) images of as-formed D2D silver nanopillars. Nanopillar formed under primary electron beam irradiation at (a) 3 keV, (b) 10 keV, and (c) 20 keV. Images were collected immediately after growth, showing nanopillars before any post-deposition treatment.

© 2026 The Author(s). Published by the Royal Society of Chemistry

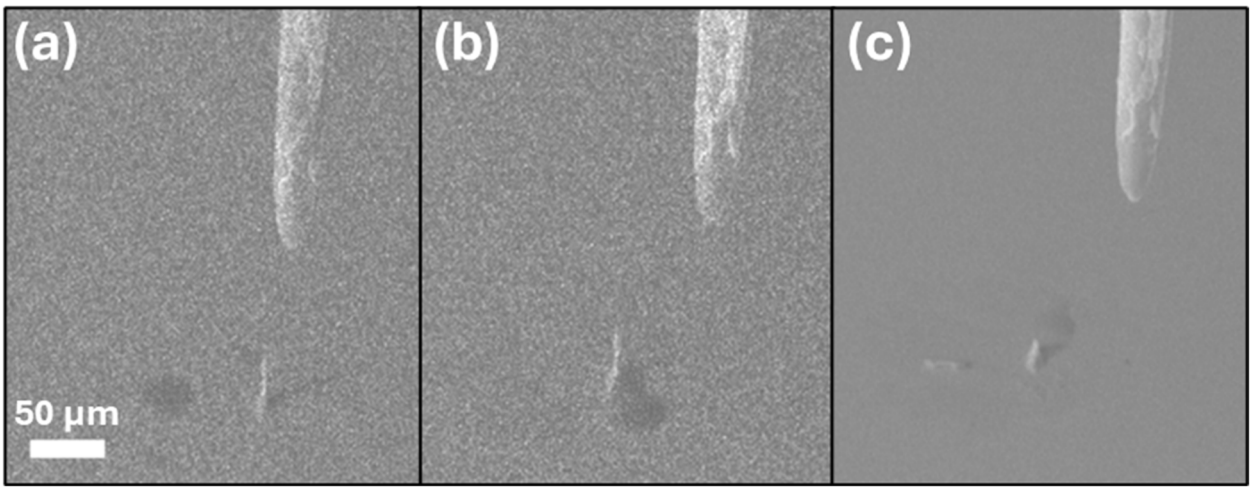


Fig. 6 SEM images of the nanobath process to remove residual salts from deposited nanopillar. A nanoelectrospray of an acetic acid and water solution is used to create a liquid film around the nanopillar for removal of residual metal salt precursor. In the "nanobath" sequence (a) the nanoelectrospray liquid film is created next to the nanopillar to tune the flow rate; (b) the emitter is moved for targeting the nanopillar by the nanoelectrosprayed solution for *in situ* cleaning the residual salts. (c) The nanopillar has broken off and fallen to the side of its original base due to forces originating from the nanoelectrospray when excessive flow is supplied.

mechanisms may also be involved, including hydrodynamic forces from the nanoelectrospray, capillary forces associated with the surrounding liquid film, and stresses generated during electron-beam-assisted growth. The relative contributions of these mechanisms were not determined in this study. After this, the acetic acid pool remains around the broken pillar and dissolves the remaining silver nitrate.

Next, the morphology of the post-nanobath nanopillars was examined to understand how electron energy affects the structure of the deposited material. The interpretations in this section are based on visual assessment of the SEM morphologies. Future crystallographic characterization using techniques such as electron backscatter diffraction (EBSD) could provide grain orientation data to further evaluate the proposed growth pathways. The nanopillar created using BSE/SE irradiation corresponding to 3 keV primary electrons is shown after nanobath treatment in Fig. 7(a). The zoomed-in BSE and SE images of the same pillar taken at 30 kV are shown in Fig. 7(b and c), respectively. The SE image shows the surface morphology of the pillar, while the BSE image provides information from a larger interaction volume within the structure. Both images show that the 3 keV nanopillar is made of densely packed nanoscale features, rather than larger grains that appear to have grown individually on the pillar. A higher magnification SE image of the same 3 keV post-nanobath pillar, marked with the dimensions of some individual features in Fig. 7(d), demonstrates representative round features with diameter of the order of few hundreds of nanometers. The image shows that the pillar is composed of round and polygonal nanoscale features, with characteristic sizes on the order of hundreds of nanometers. These features are stacked and fused together throughout the pillar body. This morphology suggests that the pillar growth at 3 keV occurs mainly by aggregation of silver nanoclusters that are already formed inside the droplets before they reach the pillar. This observation is consistent with the simulation predictions. For irradiation corresponding to 3 keV primary electrons, the calculated dose delivered to the droplet is the highest, leading to the highest rate of silver generation during droplet flight. Under this condition, the droplets are expected to form larger silver nanoclusters before landing. Because these clusters are comparatively stable, their constituent silver atoms are less likely to reorganize significantly after contact with the growing pillar, resulting in aggregation-dominated growth. The nanopillar formed under 10 keV primary electron beam irradiation, shown in Fig. 7(e–h), was imaged prior to nanobath treatment. In this case, the surface morphology of the as-grown structure was clearly visible after deposition, and therefore no additional cleaning was performed. The nanopillar created using BSE/SE irradiation corresponding to 10 keV primary electrons is shown in Fig. 7(e). Zoomed-in BSE and SE images of the same pillar, acquired at 30 kV, are shown in Fig. 7(f and g), respectively. In contrast to the 3 keV case, the zoomed-in images do not show a morphology dominated by rounded or polygonal nanoscale aggregates. Instead, the pillar contains thin, elongated features extending along the pillar body. A higher-magnification SE image of these features, with representative dimensions marked, is shown in Fig. 7(h). The elongated grains have widths close to 100 nm, while their lengths can exceed 1 μm.

The presence of these high-aspect-ratio grains suggests that the silver does not reach the pillar as large, stable round or polygonal clusters that simply stack after landing. Instead, the morphology indicates that dispersed silver atoms or smaller unstable clusters reorganize on the pillar after droplet impact along the direction of precursor delivery. This is consistent with the simulation results, which show that the dose delivered to the droplets and rate of silver creation decrease as the primary electron energy is increased. This leads to nucleation of smaller

 © 2026 The Author(s). Published by the Royal Society of Chemistry

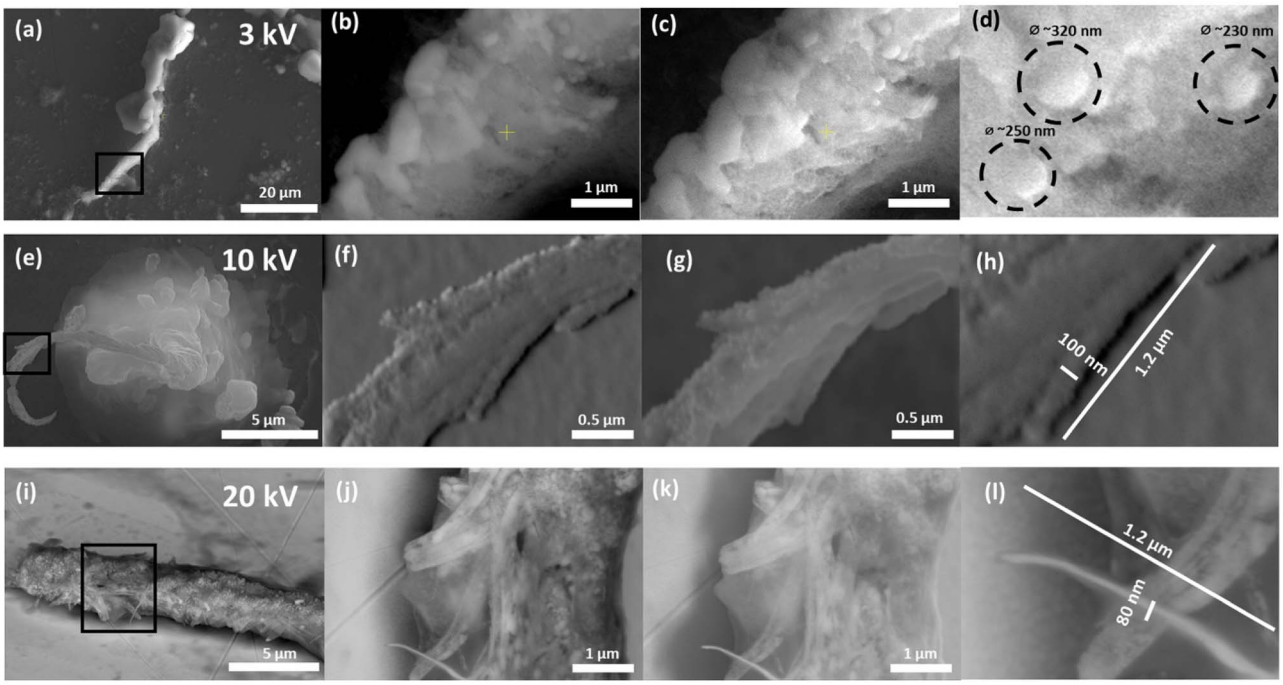


Fig. 7 Morphology of D2D nanopillars. (a) SEM image of the nanopillar created using irradiation corresponding to 3 keV primary electrons, post nanobath. (b) BSE and (c) SE images of a zoomed-in section of the same nanopillar, showing morphology consistent with aggregation of silver nanoclusters formed in the droplets. (d) Higher-magnification image of the same pillar with representative diameters of the round nanoscale features, inside dotted circles, with characteristic sizes on the order of hundreds of nanometers. (e) Nanopillar created using irradiation corresponding to 10 keV primary electrons, imaged prior to nanobath treatment. (f) BSE and (g) SE images of a zoomed-in section of the 10 keV nanopillar, showing growth of elongated linear grains on the pillar. (h) Higher-magnification image with representative dimensions of the linear grains, which have widths on the order of 100 nm and lengths that can exceed 1 µm. (i) Nanopillar created using irradiation corresponding to 20 keV primary electrons, post nanobath. (j) BSE and (k) SE images of a zoomed-in section of the 20 keV nanopillar, again showing evidence of individual grain growth and on-pillar self-organization of silver into larger linear grains. (l) Higher-magnification image of the same pillar with representative dimensions marked on an elongated grain.

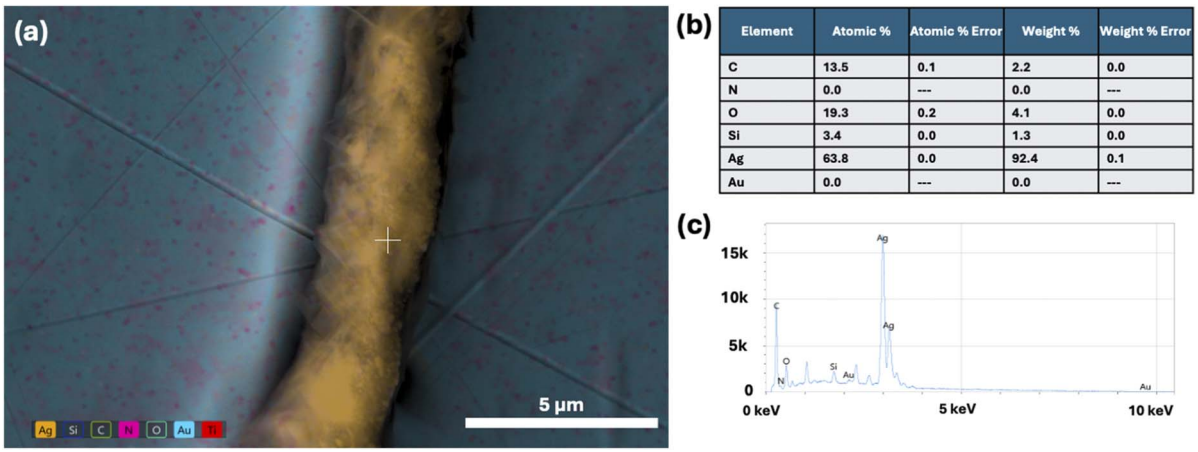
and less stable silver nanoclusters inside the droplets. After reaching the growing pillar, these smaller clusters can reorganize into lower-energy structures with preferred direction along the nanoelectrospray flow, producing the elongated grains observed in Fig. 7(f–h).

The nanopillar created using irradiation corresponding to 20 keV primary electrons is shown after nanobath treatment in Fig. 7(i). Zoomed-in BSE and SE images of the same pillar are shown in Fig. 7(j and k), respectively. Similar to the 10 keV case, the structure contains elongated features rather than round or polygonal aggregates. A higher-magnification image, with representative grain dimensions marked, is shown in Fig. 7(l). The thickness of these features is on the order of 100 nm, while their lengths can exceed 1 µm. The features observed in Fig. 7 are discussed as morphological differences and not as direct evidence of crystallographic structure or ordering.

Similar elongated features are observed in both the pre-nanobath 10 keV structure and the post-nanobath 20 keV structure, supporting the interpretation that the elongated morphology develops during growth and is not an artifact of subsequent nanobath treatment. The presence of these elongated grains again suggests that the pillar is not formed simply by stacking large silver nanoclusters created inside the droplets. Instead, the morphology is consistent with silver reaching the pillar as smaller clusters or dispersed atoms that can reorganize after landing and grow into elongated grains on the pillar surface under the influence of strong directionality of the electric field induced by the nanoelectrospray process. This observation follows the trend suggested by the simulations and supports the proposed transition from aggregation-dominated growth at lower electron energy to electric field induced on-pillar reorganization at higher electron energy.

Elemental characterization of the post-wash D2D nanopillar was performed using energy-dispersive X-ray spectroscopy (EDX), Fig. 8. The elemental map shows a silver-rich pillar, shown in yellow, placed on a gold substrate, shown in cyan, Fig. 8(a). The EDX spectrum taken at the location marked by the yellow cross in Fig. 8(a) is plotted in Fig. 8(c). The corresponding elemental percentages are shown in Fig. 8(b). The EDX results show that the pillar has a high silver content. The absence of a nitrogen signal in the selected point spectrum on the nanopillar indicates that the silver nitrate salt was effectively removed by the acetic acid nanobath process. The carbon signal in the nanopillar can be attributed to hydrocarbon residuals due to the use of acetic acid for nanobath. These results show that BSE-D2D can be used to create high-aspect-ratio, metal-rich nanostructures, while also providing control over their morphology.

© 2026 The Author(s). Published by the Royal Society of Chemistry



Element	Atomic %	Atomic % Error	Weight %	Weight % Error
C	13.5	0.1	2.2	0.0
N	0.0	---	0.0	---
O	19.3	0.2	4.1	0.0
Si	3.4	0.0	1.3	0.0
Ag	63.8	0.0	92.4	0.1
Au	0.0	---	0.0	---

Fig. 8 Elemental characterization of a D2D-fabricated silver nanopillar post-nanobath. (a) Elemental map showing the silver-rich nanopillar on the gold substrate. The yellow cross marks the location where the EDX spectrum was acquired. (b) Elemental percentages obtained from the selected point on the nanopillar. (c) EDX spectrum from the same location, showing a strong Ag signal and no detectable nitrogen signal after removal of residual silver nitrate by the nanobath process.

Conclusions

The main advancement of this work is the development of a BSE-D2D technique that enables the growth of high-aspect-ratio metal nanopillars beyond the height and angular orientation restrictions imposed by stationary liquid films in conventional LP-FEBID. A nanoelectrospray is used to deliver liquid droplets in a confined jet toward a grounded substrate inside a SEM vacuum chamber. The droplets are irradiated primarily by backscattered electrons emitted from the substrate upon exposure to the scanning high energy primary electron beam. This triggers radiolysis within the droplets and leads to reduction of metal ions/ion-complexes to metal atoms. As the droplets reach the substrate, the reduced metal accumulates on the substrate, leading to formation of high aspect ratio nanopillars in the direction of the nanoelectrospray, with the height no longer limited by the thickness of a liquid film.

The combined electron and species transport simulations show that lower primary electron beam energies deliver a higher BSE dose to the droplets and lead to a higher rate of metal ion/ion-complex reduction resulting in electrochemical synthesis of the metal phase. This suggests that lower primary electron beam energy leads to formation of larger metal nanoclusters inside the droplets. These clusters aggregate after reaching the substrate and produce a nanopillar structure dominated by omnidirectional nanocluster stacking. At higher primary electron beam energies, the BSE dose delivered to the droplets is lower and less metal is created during flight. Under these conditions, smaller metal nanoclusters and mostly dispersed metal atoms reach the growing pillar and can reorganize into lower-energy configurations along the direction of the electric field induced by nanoelectrospray, leading to creation of long elongated grains shaped by on-pillar metal atom self-organization. The experimental results follow the trend predicted by simulations. Nanopillars deposited at lower electron energy showed morphology consistent with aggregation of nanoclusters formed inside the droplets, while nanopillars deposited at higher electron energies showed evidence of on-pillar self-organization and elongated grain formation.

The acetic acid nanobath post-deposition wash was developed to remove residual metal salt from the deposited structures using the same nanoelectrospray process that is being used for delivery of the precursor salt without leaving the deposition environment. EDX analysis confirmed metal-rich nanopillars post-nanobath.

This work demonstrates the BSE-D2D process using silver nitrate as the precursor. In principle, the process could also be extended to other metal-ion precursors. Previous LP-FEBID studies have shown the feasibility of depositing metals such as copper through similar liquid-phase electron-beam-mediated processes.[18] However, extending BSE-D2D to other metals will require selection and optimization of the precursor, solvent chemistry, metal-ion complexation, and electron-beam conditions so that a sufficiently high net reduction rate can be achieved during the short droplet flight time.

The ability to sustain out of plane nanostructure growth provides a route toward fabrication of high aspect ratio conductive structures with variable angle off the substrate for three-dimensional interconnects, electrodes, field-emission devices, and sensing applications. The present study demonstrates the fundamentals of the growth process using nanopillars, but further control over the dimensions, morphology, and growth trajectory will require process maps relating electron beam energy and current, emitter geometry, precursor concentration, droplet delivery conditions, and substrate properties to the resulting deposits.

Author contributions

Auwais Ahmed: conceptualization, methodology, investigation, formal analysis, Simulation, visualization, writing – original draft, review & editing. Muhamad Zakaria: methodology,

© 2026 The Author(s). Published by the Royal Society of Chemistry

investigation, validation, formal analysis, visualization, writing – original draft. Andrei G. Fedorov: conceptualization, methodology, formal analysis, supervision, project administration, funding acquisition, writing – review & editing.

Conflicts of interest

The authors declare no conflict of interest.

Data availability

The data that support the findings of this study are available in the supplementary information (SI) of this article. Supplementary information: the detailed experimental procedures, an SEM image of the nanoelectrospray emitter (Fig. S1), the droplet time-of-flight estimate, and four videos showing nanopillar growth during the BSE-D2D process and the nanobath removal of residual salt. See DOI: https://doi.org/10.1039/d6na00760k.

Acknowledgements

This work was supported by the U.S. Department of Energy (DOE), Office of Science, Basic Energy Sciences (BES), under Award #DE-SC0010729.

References

1 V. Reisecker, R. Winkler and H. Plank, A Review on Direct-Write Nanoprinting of Functional 3D Structures with Focused Electron Beams, *Adv. Funct. Mater.*, 2024, **34**(46), 2407567.
2 S. Hari, P. H. F. Trompenaars, J. J. L. Mulders, P. Kruit and C. W. Hagen, Combined Focused Electron Beam-Induced Deposition and Etching for the Patterning of Dense Lines without Interconnecting Material, *Micromachines*, 2021, **12**(1), 8.
3 W. G. Carden, H. Lu, J. A. Spencer, D. H. Fairbrother and L. McElwee-White, Mechanism-based design of precursors for focused electron beam-induced deposition, *MRS Commun.*, 2018, **8**(2), 343–357.
4 A. G. Fedorov, S. Kim, M. Henry, D. Kulkarni and V. V. Tsukruk, Focused-electron-beam-induced processing (FEBIP) for emerging applications in carbon nanoelectronics, *Appl. Phys. A*, 2014, **117**(4), 1659–1674.
5 C. Faccini de Lima, P. Thamizhavel and T. J. Woehl, Electron–Matter Interactions During Electron Beam Nanopatterning, *Adv. Funct. Mater.*, 2026, **36**(21), e21859.
6 C. Magén, J. Pablo-Navarro and J. M. De Teresa, Focused-Electron-Beam Engineering of 3D Magnetic Nanowires, *Nanomaterials*, 2021, **11**(2), 402.
7 V. Reisecker, D. Kuhness, G. Haberfehlner, M. Brugger-Hatzl, R. Winkler, A. Weitzer, D. Loibner, M. Dienstleder, G. Kothleitner and H. Plank, Spectral Tuning of Plasmonic Activity in 3D Nanostructures *via* High-Precision Nano-Printing, *Adv. Funct. Mater.*, 2024, **34**(7), 2310110.
8 J. Lasseter, P. D. Rack and S. J. Randolph, Selected Area Deposition of High Purity Gold for Functional 3D Architectures, *Nanomaterials*, 2023, **13**(4), 757.
9 L. Berger, K. Madajska, I. B. Szymanska, K. Höflich, M. N. Polyakov, J. Jurczyk, C. Guerra-Nuñez and I. Utke, Gas-assisted silver deposition with a focused electron beam, *Beilstein J. Nanotechnol.*, 2018, **9**, 224–232.
10 L. Berger, J. Jurczyk, K. Madajska, T. E. J. Edwards, I. Szymańska, P. Hoffmann and I. Utke, High-Purity Copper Structures from a Perfluorinated Copper Carboxylate Using Focused Electron Beam Induced Deposition and Post-Purification, *ACS Appl. Electron. Mater.*, 2020, **2**(7), 1989–1996.
11 E. Bilgilisoy, J. C. Yu, C. Preischl, L. McElwee-White, H. P. Steinrück and H. Marbach, Nanoscale Ruthenium-Containing Deposits from $Ru(CO)_4I_2$ *via* Simultaneous Focused Electron Beam-Induced Deposition and Etching in Ultrahigh Vacuum: Mask Repair in Extreme Ultraviolet Lithography and Beyond, *ACS Appl. Nano Mater.*, 2022, **5**(3), 3855–3865.
12 R. Winkler, J. D. Fowlkes, P. D. Rack and H. Plank, 3D nanoprinting *via* focused electron beams, *J. Appl. Phys.*, 2019, **125**(21), 210901.
13 M. R. Henry, S. Kim and A. G. Fedorov, High Purity Tungsten Nanostructures *via* Focused Electron Beam Induced Deposition with Carrier Gas Assisted Supersonic Jet Delivery of Organometallic Precursors, *J. Phys. Chem. C*, 2016, **120**(19), 10584–10590.
14 T. J. Woehl and P. Abellan, Defining the radiation chemistry during liquid cell electron microscopy to enable visualization of nanomaterial growth and degradation dynamics, *J. Microsc.*, 2017, **265**(2), 135–147.
15 E. U. Donev and J. T. Hastings, Electron-Beam-Induced Deposition of Platinum from a Liquid Precursor, *Nano Lett.*, 2009, **9**(7), 2715–2718.
16 M. Bresin, A. Botman, S. J. Randolph, M. Straw and J. T. Hastings, Liquid phase electron-beam-induced deposition on bulk substrates using environmental scanning electron microscopy, *Microsc. Microanal.*, 2014, **20**(2), 376–384.
17 S. J. Randolph, A. Botman and M. Toth, Capsule-free fluid delivery and beam-induced electrodeposition in a scanning electron microscope, *RSC Adv.*, 2013, **3**(43), 20016–20023.
18 S. Esfandiarpour, L. Boehme and J. T. Hastings, Focused electron beam induced deposition of copper with high resolution and purity from aqueous solutions, *Nanotechnology*, 2017, **28**(12), 125301.
19 A. Ahmed and A. G. Fedorov, Peak-in-Valley Metal Nano-Architectures *via* E-Beam-Guided Metal Oxide Redox, *Adv. Funct. Mater.*, 2025, e14610.
20 J. S. Fisher, P. A. Kottke, S. Kim and A. G. Fedorov, Rapid electron beam writing of topologically complex 3D nanostructures using liquid phase precursor, *Nano Lett.*, 2015, **15**(12), 8385–8391.
21 J. S. Fisher, P. A. Kottke and A. G. Fedorov, Synthesis of crystalline metal nanomonoliths by e-beam reduction of negatively electrified jets, *Mater. Today Phys.*, 2018, **5**, 87–92.

© 2026 The Author(s). Published by the Royal Society of Chemistry

22 A. Ahmed, E. C. Boyle, P. A. Kottke and A. G. Fedorov, Radiolytic redox interplay defines nanomaterial synthesis in liquids, *Sci. Adv.*, 2021, **7**(51), eabj8751.
23 A. Ahmed, P. A. Kottke and A. G. Fedorov, Electrochemical Lensing for High Resolution Nanostructure Synthesis in Liquids, *ACS Appl. Nano Mater.*, 2024, **7**(13), 15438–15445.
24 B. Fritsch, S. Lee, A. Körner, N. M. Schneider, F. M. Ross and A. Hutzler, The Influence of Ionizing Radiation on Quantification for *In Situ* and Operando Liquid-Phase Electron Microscopy, *Adv. Mater.*, 2025, **37**(13), 2415728.
25 J. Sun, B. Fritsch, A. Körner, M. Taherkhani, C. Park, M. Wang, A. Hutzler and T. J. Woehl, Discovery of molecular intermediates and nonclassical nanoparticle formation mechanisms by liquid phase electron microscopy and reaction throughput analysis, *Small Struct.*, 2024, **5**(10), 2400146.

© 2026 The Author(s). Published by the Royal Society of Chemistry